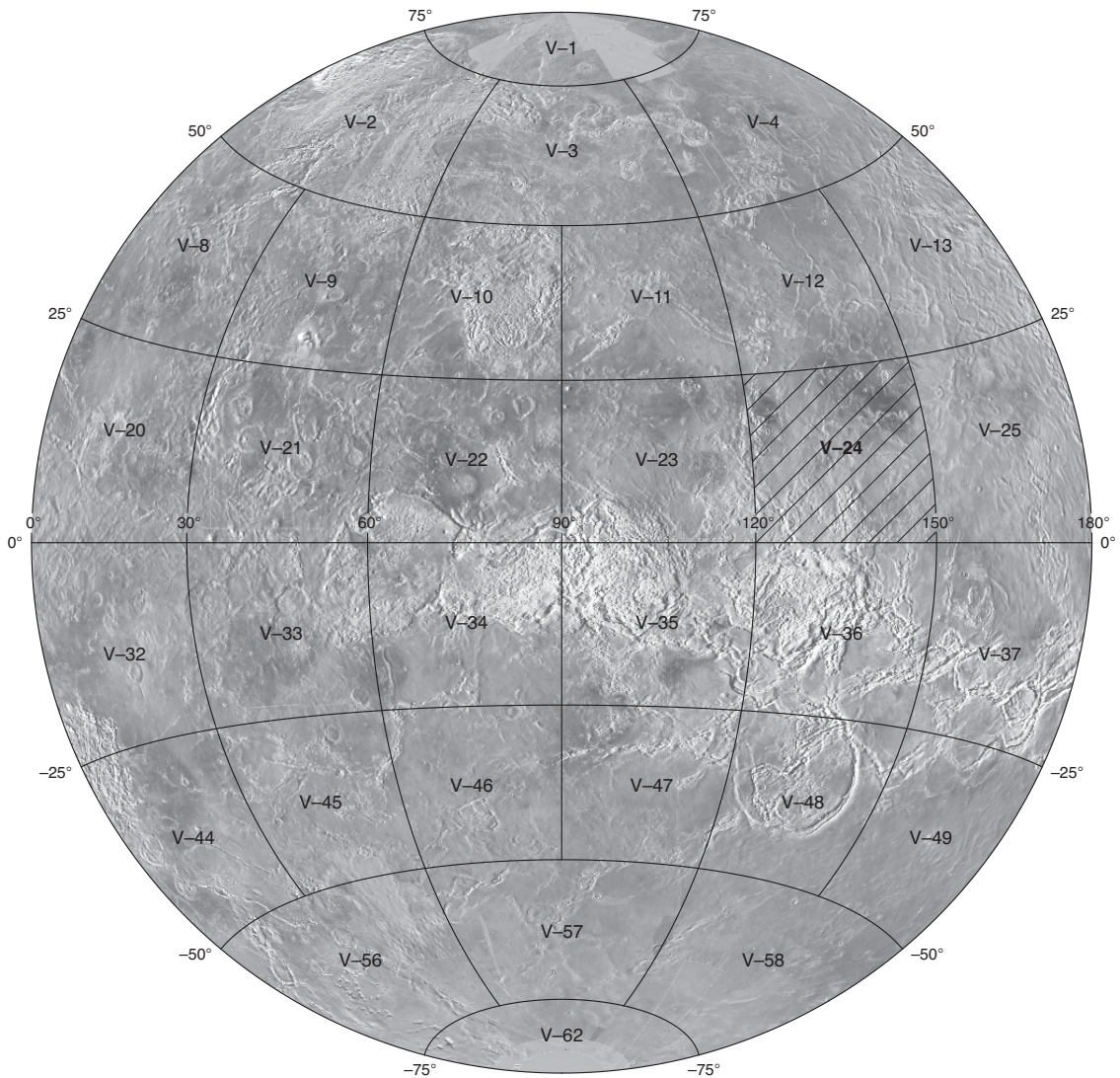


Prepared for the National Aeronautics and Space Administration

Geologic Map of the Greenaway Quadrangle (V-24), Venus

By Nicholas P. Lang and Vicki L. Hansen

Pamphlet to accompany
Scientific Investigations Map 3089



2010

U.S. Department of the Interior
U.S. Geological Survey

Contents

The Magellan Mission	1
Magellan Radar Data	1
Introduction	1
Data	2
Terminology	2
Mapping Techniques and SAR Image Interpretation	2
Geology of the Greenaway Quadrangle (V-24)	3
Geologic Overview	3
Geologic Units	3
Terrain and Flow Materials	3
Ribbon-Tessera Terrain	3
Intratessera Basin Material	5
Lineated Terrain	5
Shield Terrain	5
Coronae-Sourced Flow Material	6
Impact Craters	6
Channels	7
Simple Channels	7
Complex Channels	7
Tectonic Features	7
Wrinkle Ridges	7
Linear Features	7
Coronae	8
Dorsa	9
Discussion	9
Geologic History.....	10
References Cited.....	11

Table

1. Crater data for the Greenaway quadrangle (V-24), Venus	15
---	----

The Magellan Mission

The Magellan spacecraft orbited Venus from August 10, 1990, until it plunged into the Venusian atmosphere on October 12, 1994. Magellan Mission objectives included (1) improving the knowledge of the geological processes, surface properties, and geologic history of Venus by analysis of surface radar characteristics, topography, and morphology and (2) improving the knowledge of the geophysics of Venus by analysis of Venusian gravity.

The Magellan spacecraft carried a 12.6-cm radar system to map the surface of Venus. The transmitter and receiver systems were used to collect three data sets: (1) synthetic aperture radar (SAR) images of the surface, (2) passive microwave thermal emission observations, and (3) measurements of the backscattered power at small angles of incidence, which were processed to yield altimetric data. Radar imaging and altimetric and radiometric mapping of the Venusian surface were accomplished in mission cycles 1, 2, and 3 from September 1990 until September 1992. Ninety-eight percent of the surface was mapped with radar resolution on the order of 120 m. The SAR observations were projected to a 75-m nominal horizontal resolution, and these full-resolution data compose the image base used in geologic mapping. The primary polarization mode was horizontal-transmit, horizontal-receive (HH), but additional data for selected areas were collected for the vertical polarization sense. Incidence angles varied between about 20° and 45°.

High-resolution Doppler tracking of the spacecraft took place from September 1992 through October 1994 (mission cycles 4, 5, 6). Approximately 950 orbits of high-resolution gravity observations were obtained between September 1992 and May 1993 while Magellan was in an elliptical orbit with a periapsis near 175 km and an apoapsis near 8,000 km. An additional 1,500 orbits were obtained following orbit-circularization in mid-1993. These data exist as a 75° by 75° harmonic field.

Magellan Radar Data

Radar backscatter power is determined by (1) the morphology of the surface at a broad range of scales and (2) the intrinsic reflectivity, or dielectric constant, of the material. Topography at scales of several meters and larger can produce quasi-specular echoes, and the strength of the return is greatest when the local surface is perpendicular to the incident beam. This type of scattering is most important at very small angles of incidence, because natural surfaces generally have few large tilted facets at high angles. The exception is in areas of steep slopes, such as ridges or rift zones, where favorably tilted terrain can produce very bright signatures in the radar image. For most other areas, diffuse echoes from roughness at scales comparable to the radar wavelength are responsible for variations in the SAR return. In either case, the echo strength is also modulated by the reflectivity of the surface material. The density of the upper few wavelengths of the surface can have a significant effect. Low-density layers, such as crater ejecta or volcanic ash, can absorb the incident energy and produce a lower observed echo. On Venus, a rapid increase in reflectivity exists at a certain critical elevation

above which high-dielectric minerals or coatings are thought to be present. This leads to very bright SAR echoes from virtually all areas above that critical elevation.

The measurements of passive thermal emission from Venus, though of much lower spatial resolution than the SAR data, are more sensitive to changes in the dielectric constant of the surface than to roughness. They can be used to augment studies of the surface and to discriminate between roughness and reflectivity effects. Observations of the near-nadir backscatter power, collected using a separate smaller antenna on the spacecraft, were modeled using the Hagfors expression for echoes from gently undulating surfaces to yield estimates of planetary radius, Fresnel reflectivity, and root-mean-square (rms) slope. The topographic data produced by this technique have horizontal footprint sizes of about 10 km near periapsis and a vertical resolution on the order of 100 m. The Fresnel reflectivity data provide a comparison to the emissivity maps, and the rms slope parameter is an indicator of the surface tilts, which contribute to the quasi-specular scattering component.

Introduction

The Greenaway quadrangle (V-24; lat 0°–25° N., long 120°–150° E.), Venus, derives its name from the impact crater Greenaway, centered at lat 22.9° N., long 145.1° E., in the northeastern part of the quadrangle. Greenaway was a well-noted writer and illustrator of children's books in Britain during the nineteenth century. In Greenaway's honor, the Library Association of Great Britain presents the annual Kate Greenaway Medal to an illustrator living and publishing in Britain who has produced the most distinguished children's book illustrations for that year.

The Greenaway quadrangle occupies an 8,400,000 km² equatorial swath of lowlands and highlands (fig. 1). The map area is bounded by the crustal plateau, Thetis Regio, to the south and Gegute Tessera to the west. The rest of the quadrangle consists of part of Llorona Planitia, which is part of the vast lowlands that cover about 80 percent of Venus' surface (Masursky and others, 1980). The southern map area marks the north edge of Aphrodite Terra, including Thetis Regio, that includes the highest topography in the quadrangle with elevations reaching >1 km above the Mean Planetary Radius (MPR; 6,051.84 km). Northern Aphrodite Terra abruptly slopes north to Llorona Planitia. A broad northeast-trending topographic arch pocked with coronae separates two northeast-trending elongate basins, Llorona Planitia on the east, that form depositional centers for shield and coronae-sourced materials; both basins drop to elevations of <-1 km. In addition to these major features, the map area hosts thousands of small volcanic constructs (shields); seven coronae; ribbon-tessera terrain; suites of faults, fractures, and wrinkle ridges; 23 impact craters; and one craterless splotch.

Our goal for mapping the geology of the Greenaway quadrangle was to determine the geologic history for this region, which in turn provides insights into volcanic and tectonic processes that shaped the Venusian surface. Map relations illustrate

that aerially expansive shield terrain (unit *st*; see Aubele, 1996; Hansen, 2005) played a primary role and coronae played a secondary role in volcanic resurfacing across the map area.

Data

Mapping was conducted using cycles 1, 2, and 3 of NASA Magellan synthetic aperture radar (SAR) imagery and Magellan altimetry datasets. We compiled the map on a digital C-1MIDR (Compressed Once Mosaiced Image Data Record) 225-m/pixel SAR base, however we mapped using full-resolution, hard-copy images and full-resolution digital (~100 m/pixel) normal and inverted (negative) SAR image bases. Synthetic stereo imagery, created by merging altimetry data with cycle 1 SAR (Kirk and others, 1992), using NIH-Image macros developed by D.A. Young, proved useful in resolving the interactions of flows, primary and secondary structures, and topography. In addition, we incorporated emissivity, reflectivity, and rms-slope data sets for V-24 to aid in mapping as necessary (fig. 2). Adobe Illustrator™ 9 and 10, in association with Avenza MAPublisher™ 4, comprised the primary mapping and GIS tools; we enhanced radar images using Adobe Photoshop™ 5. We obtained digital full-resolution SAR image bases from the U.S. Geological Survey MAP-A-PLANET website (<http://www.mapplanet.org>).

Terminology

Because terminology can carry stated and unstated assumptions that may vary with the reader or through time, we use this section to define terminology used herein.

We use the term “geologic unit” to mean a body of rock that consists of dominant, unifying features recognizable in the Magellan SAR imagery and mappable at the 1:5,000,000 scale. Primary and secondary structures play critical roles in geologic-unit identification. Primary structures form during unit emplacement and include channels, flow boundaries, and volcanic edifices (shields). Secondary, or tectonic (strain), structures form after unit emplacement and include deformation features such as faults, fractures, ridges, folds, lineaments, and ribbon structures—parallel, paired, radar-bright and radar-dark lineaments that define a periodic fabric marked by parallel extensional troughs and ridges and have large length:width aspect ratios (Hansen and Willis, 1996, 1998; Ghent and Hansen, 1999).

We separate geologic units into material units and terrains. The term “material unit” describes a sequence of materials interpreted to have been emplaced during a specific period of geologic time or representing a specific process. For example, corona-related flow material represents specific material emplaced during one or multiple volcanic eruptions; impact-crater ejecta deposits represent a specific process. The term “terrain” describes a texturally defined region (Hansen, 2005). The texture could include primary or secondary structures and imply that a particular region experienced at least one event that melded possibly previously unrelated material units (any combination of igneous, metamorphic, and sedimentary rocks) into a new package; this new package may be a larger collection

of preserved material units (shield terrain, unit *st*) or a region characterized by secondary (tectonic) structures (Llorona Planitia lineated terrain, unit *IL*). There is no implication of a unique history prior to the event(s) that melded potentially separate units into the textural terrain. Events prior to terrain formation are unconstrained unless specifically noted. Gneissic terrain represents an analogous terrestrial unit.

Terrains in the map area include shield terrain, ribbon-tessera terrain, and a lineated terrain. Ribbon-tessera terrain and lineated terrain are each defined by secondary structures indicating that the host material(s) forming each terrain underwent a shared deformation history that completely inhibits original unit identification (Wilhelms, 1990). Shield terrain differs from ribbon-tessera terrain and lineated terrain in that it represents a shared emplacement mechanism (represented by primary structures). Shield terrain is comparable, for example, to a terrestrial sedimentary formation comprised of turbidite deposits from multiple source regions. Absolute time involved in shield terrain formation is unconstrained, whereas a terrestrial turbidite terrain might have many accessible clues to temporal evolution. Terrains, whether marked by shared tectonic histories or depositional histories, may represent multiple, time transgressive, events; timing across an entire terrain cannot be assumed.

The term “lowland” is used in a topographic sense in reference to broad, regional, long-wavelength (approximately hundreds of kilometers) basins. The terms “planitia” (singular) or “planitiae” (plural), used in a geomorphic sense, refer to individual basins or lowland regions (Llorona Planitia).

Mapping Techniques and SAR Image Interpretation

The first order task in mapping geologic units is to determine their spatial distribution and to examine their contact relations with adjacent units (Wilhelms, 1990). Using Magellan SAR imagery, we identify geologic units on Venus using the following criteria: patterns in SAR, identification of sharp continuous contacts, interaction with or truncation of underlying structures, and (or) the presence of primary structures. These criteria allow determination of a reasonable geologic history and hint at a three-dimensional geometry (for further discussion see Wilhelms, 1990; Tanaka and others, 1994; Hansen, 2000; Zimbelman, 2001; Skinner and Tanaka, 2003). The radar dataset, however, may inhibit unique distinction between geologic units because radar backscatter is sensitive to surface roughness at the scale of radar wavelength (Ford and others, 1993). Such roughness differences could be attributed to facies changes within a single unit, such as the transition from pahoehoe to aa facies within an individual terrestrial lava flow; pahoehoe facies exhibit low-radar backscatter, whereas aa facies may display high-radar backscatter. Mapping geologic units solely on radar backscatter would incorrectly delineate such a flow into two separate geologic units. Hence, the truncation of structures and (or) the presence of distinctive patterns in primary structures are the most reliable criteria for identifying geologic units. Where possible, we indicate flow direction; arrows indicate both the interpreted flow direction and the location of flows, providing locations

of substantive evidence for minimum limits of flow units. Hachured lines indicate the extent of a flow front. Thin dashed lines indicate that unit contacts are approximately located due to vague outcrop expression. Thick dashed lines indicate a gradational boundary where the transition between units may exist over several tens to hundreds of kilometers. Radar boundaries indicate the locations of sharp, radar-backscatter transitions in the lowlands. Based on caveats discussed above, it is unclear if the radar boundary represents a geologic boundary. When mapping secondary structures, we do not map every single structure observed on the SAR imagery. Instead, we map a representative amount of each structure to convey the density and distribution of individual suites. In many cases, the exact location of a unit contact or the total number of structures is most important within the context of specific questions. Thus, we encourage users of this map to examine such contacts and distribution of structures in detail with specific questions in mind.

One major limitation in interpreting the geologic history of Venus' surface is the uncertainty of rock types. We assume that Venus could host only the three basic rock types observed on Earth: igneous, metamorphic, and sedimentary. The extremely dehydrated state of the lower atmosphere (Donahue and others, 1997) and lithosphere (Mackwell and others, 1998), as well as the high current surface temperature of approximately 460°C (Crisp and Titov, 1997), precludes the current presence of surface water, dismissing the idea that many surface rocks are sedimentary. In addition, the apparent absence of widespread erosion suggests that surface rocks are not likely exposed crustal metamorphic rocks or intrusive igneous rocks. Thus, surface rocks most likely originated as extrusive igneous (volcanic) rocks (Banerdt and others, 1997), an interpretation consistent with the abundance of volcano-like features on Venus (Head and others, 1992) and geochemical measurements of a basaltic surface composition (Grimm and Hess, 1997). Exceptions to volcanic rocks on Venus include impact-related materials (Schultz, 1992; Campbell and others, 1992), eolian deposits (Arvidson and others, 1992; Greeley and others, 1992), and atmospheric chemical precipitates (Fegley and others, 1997). Although these materials are present on Venus, their aerial extent appears limited. However, given the uncertainty of past Venus climatic conditions (Bullock and Grinspoon, 1996; Donahue and others, 1997; Phillips and others, 2001) and our nascent understanding of Venusian surface processes, it is best to keep an open mind when interpreting Venus' rock record. Venus could indeed have hosted vast oceans in the past (Donahue and others, 1982; Donahue and Russell, 1997; Donahue, 1999; Hunten, 2002; see also Jones and Pickering, 2003; Hamilton, 2005).

Geology of the Greenaway Quadrangle (V-24)

Geologic Overview

Geologic units in the Greenaway quadrangle include three terrain units and 11 material units. Terrain units characterize most of the map area and include a regionally expansive shield-

dominated terrain (unit **st**), a ribbon-tessera terrain (unit **rtGH**), and a potentially regionally extensive lineated terrain (unit **ll**) characterized by closely spaced (<<1 km), northwest-trending lineaments. Interspersed with the terrains are material units separated into flow materials (presumed volcanic and associated mostly with individual coronae) and materials associated with impact craters. Coronae-related materials include coronae-sourced flow materials. Impact-crater materials are mapped as undivided ejecta (unit **cu**), fluidized outflow (unit **co**), and crater fill (unit **cf**). One terrain unit (unit **st**) and one of the material units (unit **fu**) are composite units composed of multiple flows emplaced over an unknown period of geologic time; we considered them stratigraphically discontinuous units.

The map area also hosts an array of secondary structures. Secondary structures occur at a variety of scales and include fractures, folds, ridges, and lineaments. Multiple suites of structures locally occur together to structurally define larger scale features, such as coronae, as well as individual suites defining features such as fracture zones. Wrinkle ridges trend mostly east-northeast across the northern one-third of the quadrangle, where they deform a majority of the map units located in the lowlands. Local deviations from the dominant northeast trend occur and are apparently associated with local features. For example, wrinkle ridges near lat 18.5° N., long 131.5° E. make an arcuate bend along the northwest margin of a corona-like feature.

The geology and topography in the map area are grossly linked. Crustal-plateau (high-standing, flat-topped, quasi-circular regions interpreted as isostatically supported by relatively shallow low-density material [Bindschadler and others, 1992; Phillips and Hansen, 1994; Hansen and others, 1997]), ribbon-tessera terrain characterizes the highlands along the west and south boundaries of the map area. Local topographic highs as much as approximately hundreds of meters in elevation occur across the quadrangle and mark kipukas of ribbon-tessera terrain and unit **ll**. Shield terrain dominates most of the lowland where it embays units **rtGH** and **ll** (fig. 3). A northeast-trending topographic arch marked by four coronae divides the lowland into two topographic basins. The western basin hosts local outcroppings of unit **ll**, as well as three separate units of flow material (units **fcA**, **fcR**, **fcS**) that broadly parallel the basin trend. The eastern basin hosts extensive outcrops of unit **ll**. Corona-sourced flow material is present along the northeast margin of the eastern basin (unit **fcI**). Coronae along the topographic arch produced flow material that has embayed kipukas of unit **rtGH** located along the arch flanks.

Geologic Units

Terrain and Flow Materials

Ribbon-Tessera Terrain

Ribbon-tessera terrain is defined as deformed crust containing multiple suites of intersecting tectonic structures including folded-ribbon structures (Hansen and Willis, 1996). Ribbon-tessera terrain includes two large ribbon-tessera inliers (Gegute and Haattse-baad Tesserae) and kipukas that crop out

across the map area. Gegute Tessera, located along the west boundary of V-24, is a large arcuate inlier that reflects a broad, north-trending warp; the inlier grades into smaller outcrops, or kipukas, along its margins. Haastse-baad Tessera occurs along the south margin of the map and marks the northeast edge of Aphrodite Terra. This region includes numerous blocks separated by topographic lows marked with low-backscatter material mapped as unit *st* and flow material associated with Blai and Rosmerta Coronae (units *fcB*, *fcR*). We map ribbon-tessera terrain (unit *rtGH*) as a single unit, based on the similarity of structure trends present in all tessera outcrops. However, unit *rtGH* should not be viewed as a synchronously formed geologic unit but as an indeterminate (one or many) number of pre-existing materials subsequently deformed one or multiple times.

Numerous secondary structures recognized as ribbon structures, folds, and lineaments characterize unit *rtGH* in the map area. The structures occur at scales from an effective image resolution of about 1 km to tens of kilometers (fig. 4) across all of unit *rtGH* and have erased the original character of the predeformation materials (Wilhelms, 1990). Clues to the type of material and emplacement style of the pre-ribbon-tessera materials are subsequently indeterminate due to ribbon-tessera deformation. Because structure wavelengths extend to effective image resolution, it is conceivable that they may extend below effective image resolution (Zimbelman, 2001). Figure 4 highlights the southwest corner of the Haastse-baad Tessera region and serves as an example of both the abundance of ribbon-tessera structures and the various wavelengths at which they can occur within unit *rtGH*. Six types of secondary structures characteristic of unit *rtGH* are highlighted in figure 4. These structures include a northeast-trending background fabric, a suite of northwest-trending ribbon structures (wavelength approximately 2.5 km), northwest-trending parallel folds or warps (wavelength approximately 15–20 km) that occur at oblique angles to ribbon structures, two types of ribbon-tessera lineaments, and structural troughs associated with basin and dome terrain (Hansen and Willis, 1996). Ribbon structures occur across all of unit *rtGH* and have both northwest and orthogonal northeast trends. Long-wavelength folds or warps also locally occur within the northwestern (northwest-trending folds with wavelengths of 15–25 km) and eastern (north-northeast-trending folds with wavelengths of 15–20 km) expanses of the Haastse-baad Tessera region. The structural troughs associated with basin dome terrain consist of linear and curvilinear ridges and troughs that deform earlier formed ribbon fabrics (fig. 4C) and occur mostly within the central region of the Haastse-baad Tessera region. Curvilinear ridges and troughs display variable trends and rounded, gentle slopes similar to a fold. It is not clear if the linear and curvilinear ridges and troughs record contractional or extensional strain. However, the curvilinear nature implies multiple episodes of deformation.

Of the secondary structures identified in figure 4, the background fabric and the two types of ribbon-tessera lineaments are worth discussing further.

The background fabric consists of lineaments that are penetrative at image resolution and that appear to be constrained to the Haastse-baad Tessera region of unit *rtGH*. The character of individual lineaments is undefined: lineaments trend northeast

with lengths as much as hundreds of kilometers and are overprinted by later-forming tessera structures.

The two distinct suites of ribbon-tessera lineaments are distinguished based on structure spacing and are termed ribbon-tessera lineament *a* and ribbon-tessera lineament *b*. Ribbon-tessera lineament *a* occurs within suites of tightly spaced ($\ll 1$ km) lineaments that define variable trends across unit *rtGH*. Within figure 4 and kipukas in eastern V-24, these lineaments define northwest and orthogonal northeast trends, however within the Gegute Tessera region, they define mostly northwest trends. Tessera lineament *a* is similar to the S-type structures identified by Tuckwell and Ghail (2003) and Kumar (2005) along the boundary between southeastern Ovda Regio and northwestern Thetis Regio. In some regions, suites of ribbon-tessera lineament *a* appear to wrap around some ribbon-tessera blocks and may represent a zone of high strain (for example, near lat 5° N., long 137° E.). At these locations, the fabric might indicate local shearing within regions of unit *rtGH*. Ribbon-tessera lineament *b* has 1–10 km spacing and broadly parallels the trends of the long-wavelength folds or warps in unit *rtGH*. The nature of ribbon-tessera lineament *b* is indeterminate, although this lineament suite may be similar to short-wavelength folds identified by Nordberg and others (2005) in Alpha Regio and by Hansen (2006) in Ovda Regio.

One other type of secondary structure, which is not observed in figure 4, also occurs in unit *rtGH*. Steep-walled structural troughs that have rectangular cross sections and a consistent width of approximately 2 km cut northern Haastse-baad Tessera and several tessera kipukas in the central map area. The troughs cut all pre-existing structures and maintain a spacing of approximately 10–50 km. Within northern Haastse-baad Tessera, these troughs describe an arcuate pattern, whereas they describe variable trends within tessera-terrain kipukas north of Haastse-baad Tessera.

Temporal relations between the various structural suites that contain ribbon-tessera terrain fabrics are constrained based on mechanical arguments. Based on figure 4B, ribbons cut the background fabric, which implies that the fabric predates ribbon structures. However, other temporal relations are not as straightforward. Ribbon-structure wavelengths, marked by ribbon-ridge width (2.5 km), suggest a shallow depth, possibly between 0.6 and 2.9 km deep (see Ghent and Tibuleac, 2002), to the brittle-ductile transition (BDT) at the time of ribbon formation (Hansen and Willis, 1998). In turn, fold wavelengths between 15 to 25 km imply a depth to BDT of approximately 6 km (Brown and Grimm, 1997; Ghent and Hansen, 1999). Northwest-trending graben with wavelengths of approximately 15–25 km (fig. 4A, C) that cut across all structures, as well as the basin and dome terrain, also imply a relatively deeper depth to BDT at the time of their formation. Based on the interpreted depth to BDT required to form the various tessera structures, it seems plausible that the structures reflect a progressive thickening of the lithosphere as the BDT moved downward with time. Therefore, ribbons and, thus, the background fabric likely formed before tessera folds, graben, and basin and dome terrain. If ribbons and the background fabric formed after the folds, the shallow BDT would not support the folds, and they would have disappeared by viscous relaxation (Hansen and Willis, 1998).

Relative timing between the formation of folds and basin and dome terrain is unconstrained. The northwest-trending graben crosscut and, therefore, postdate all the other structures. Hansen (2006) also presents a detailed discussion of ribbon-tessera-terrain evolution derived from detailed mapping of a portion of Ovda Regio. For a different view of the evolution of ribbon-tessera-terrain fabric, see Gilmore and others (1998).

Intratessera Basin Material

Intratessera basins, marked by local topographic lows as deep as several hundred meters, reside locally within tracts of ribbon-tessera terrain (Bindschadler and Head, 1991; Banks and Hansen, 2000). In the map area, these basins occur within Gegute and Haastse-baad Tesserae and are floored with low-radar-backscatter material (unit *ibGH*) assumed to be volcanic in origin following previous interpretations (Bindschadler and others, 1992; Gilmore and Head, 1994; Banks and Hansen, 2000; Bleamaster and Hansen, 2005). Intratessera basins in Gegute Tessera broadly mimic the inlier's arcuate nature; whereas basin shapes in Haastse-baad Tessera mimic local tectonic trends. Unit *ibGH* commonly preserves primary shield edifices and typically does not exhibit tessera-related structure, implying that unit *ibGH* postdated tessera-related tectonism. Lumping of spatially disparate unit *ibGH*, as we have done, is not meant to imply that all intratessera basins, or basin fill, formed at the same time.

Lineated Terrain

Tightly spaced ($\ll 1$ km spacing) northwest-trending lineaments characterize unit *IL*. Lineaments are predominantly fractures marked by linear topographic lows, although local ridges exist. Unit *IL* crops out across the lowland, occurring as 10- to 1,000-km² patches; the largest expanses are exposed in the eastern basin in spatial association with Barbale and Lumo Dorsa. The topographic arch hosts approximately 10 km² patches of unit *IL* in the vicinity of Kamadhenu Corona, and the western basin hosts approximately 100 km² patches in the vicinity of Gegute Tessera. Lineament trends are parallel within all unit *IL* outcrops. In addition, where unit *IL* crops out near ribbon-tessera-terrain units, lineament trends broadly parallel ribbon fabrics and tessera lineament *a* trends within unit *rtGH*. Based on this parallelism in all unit *IL* outcrops, we map the lineated terrain as a single, undivided terrain that represents materials that have experienced at least one episode of deformation. Presumably, deformation destroyed the nature of the original unit(s) and created a tectonic fabric that characterizes the lineated terrain unit. The consistent northwest trend, preserved across spatially separate exposures, indicates that unit *IL* may form a regionally expansive unit that underlies much of unit *st* and corona-sourced flow materials.

Outcrops of unit *IL* are related to the unit's low local relief that ranges from below the resolution of Magellan radar altimetry to as much as approximately hundreds of meters. Flow material associated with units *st* and *fu* flood much of unit *IL*, locally covering the topographically lowest portions and preserving the topographically highest portions of the unit. In many cases, this results in variable exposures of unit *IL* over distances of

as much as hundreds of kilometers (for example, see fig. 3). In such cases, we map the boundary between unit *IL* and embaying flow materials as a gradational contact (in plan view); we place the contact at the first exposure of unit *IL* that is mappable at the 1:5,000,000 scale. Because the contact is gradational between unit *IL* and units *st* and *fu*, flow material associated with units *st* and *fu* flood low-lying regions within areas mapped as unit *IL*. To delineate the degree of such flooding, we divided unit *IL* into two facies: facies *a* and facies *b*. Facies *a* includes extensively flooded portions of unit *IL*, whereas facies *b* includes less-flooded portions of the unit where flow material associated with units *st* and *fu* locally flood some fractures (see fig. 3*B*).

Shield Terrain

Unit *st*, shield terrain, collectively consists of shield edifices and erupted products. Shield edifices, or shields, are circular to quasi-circular features that are flat-topped or cone, dome, or shield shaped, generally $\ll 1$ km in height, and typically 1–2 km in diameter (Guest and others, 1992; Crumpler and others, 1997). A few shields range to approximately 20 km in diameter. Shields may or may not contain a summit pit. Shield size is difficult to constrain, because shield bases are typically poorly defined; shields appear to blend into the erupted products of other shields. The erupted products represent material potentially emplaced from any combination of lava flows, air-fall deposits, or pyroclastic flows (Guest and others, 1992). The erupted products, collectively called “shield paint” (Hansen, 2005), appear to have coalesced to form a coherent, mechanical layer that variably covers pre-existing materials and structures (fig. 3). The shield paint contains windows that expose the local underlying geology. Individual flows within shield paint are typically indistinguishable; based on radar caveats discussed above and the limited spatial extent of individual radar domains, we do not attempt to divide distinct individual flow units or shield clusters, even though sharp radar backscatter transitions within unit *st* may reflect flow boundaries. However, we should note that shields located within corona interiors could represent shield fields that could be associated with the evolution of individual corona (Crumpler and others, 1997).

Shield terrain displays three types of relations with other map units and features in the Greenaway quadrangle. First, units that are topographically higher than unit *st* (unit *rtGH*) display definite, abrupt boundaries with shield terrains. Second, units that have low local relief (unit *IL*) display contacts with unit *st* that exist over tens to hundreds of kilometers; there is a gradation in plan view from unit *st* to the other unit, a phenomenon illustrated in figure 3. Figure 3 illustrates shield paint that flowed into local topographic lows and around local topographic obstacles, resulting in a tight, digitate contact between younger shield paint and older lineated terrain (unit *IL*). The detail of the boundary between unit *IL* and shield terrain indicates an extremely shallow contact that is characteristic of the boundary between the two units. The complex contact also indicates that shield terrain forms a thin layer, possibly on the order of meters to tens of meters, an interpretation consistent with Guest and others (1992), who estimated shield-associated deposits as likely tens of meters or less in thickness (see also,

Hansen, 2005). The third type of relation is a time-transgressive relation, which unit *st* displays with other flow units and tectonic structures. For example, Rosmerta Corona flow material (unit *fcR*) locally covers unit *st* at lat 11° N., long 124° E. In turn, scattered shields variably occur across much of unit *fcR*. In addition, fractures locally cut unit *st* in some areas, presumably because of structural reactivation; shields and associated materials, in turn, locally cover fractures. For example, near lat 8° N., long 139° E., lineaments associated with unit *IL* cut unit *st*. In turn, the lineaments terminate along a radar-backscatter boundary.

Shield terrain is an aerially expansive unit that covers much of the map area and extends into adjoining quadrangles. Unit *st* covers >70 percent of the map area and extends north into Shimti Tessera quadrangle (V-11) and Vellamo Planitia quadrangle (V-12), where it is equivalent with the shield plains of Aubele (1996). Shield terrain also extends westward into Niobe Planitia quadrangle (V-23; Hansen, 2005, 2006), and shield densities along the borders with Rusalka Planitia quadrangle (V-25; between lats 3°–16° N.) and Thetis Regio quadrangle (V-36; between longs 142°–148° E.) suggest that unit *st* extends into these two quadrangles. However, Young and Hansen (2003) did not describe shield terrain within V-25 but instead identified several shield fields along its west border. Perhaps regionally extensive shield terrain in the map area grades into localized shield fields within V-25. Further, shield density seems to decrease dramatically in the southeast corner of the map area (near lat 1° N., long 149° E.) and gradually in the northeast corner. In the southeastern map area, unit *fc* appears to mark the boundary with unit *st*; unit *fc* may locally cover shields and related deposits associated with unit *st*. There is no obvious reason for the decrease in shield density in the northeastern map area, although the gradual decrease in shield density suggests that shield terrain grades into materials that come from other sources; as such, we map a gradational boundary from unit *st* to unit *fu*. However, it is also possible that the apparent decrease in shields can be attributed to the regional, impact-crater haloes obscuring the shields and (or) the diameters of shields in this region being below the effective resolution of Magellan imagery (Zimbelman, 2001).

Coronae-Sourced Flow Material

Corona-sourced flows in the map area vary in aerial extent. For example, units *fcA* and *fcB* form relatively localized flows that extend a few hundred kilometers or less from their sources. High-standing tracts of unit *rtGH* locally limit the extent of unit *fcB*. In contrast, units *fcR*, *fcS*, and *fcI* define relatively extensive corona-sourced flows that extend greater than 300 km from their source. Unit *fcR*, the most expansive corona flow in the map area, floods much of the Haastse-baad Tessera region of unit *rtGH* and spills into three adjoining quadrangles: Niobe Planitia (V-23; Hansen, 2009), Ovda Regio (V-35; Bleamaster and Hansen, 2005), and Thetis Regio (V-36). Flow directions and flow fronts preserve a record of flow directions within unit *fcR*. Rosmerta Corona flows may have traversed through a fracture zone north of Rosmerta Corona and into the western basin where flow limits become difficult to define. A possible

flow-front limit is indicated on the map, although changes in radar backscatter characteristics north of this boundary indicate that the flow might extend farther north. Unit *fcS*, forming a relatively narrow lobate flow approximately 700 km long within the map area, extends from Vellamo Planitia quadrangle (V-12) and broadly parallels the trend of the western basin; the source of unit *fcS* is uncertain, but it may be Boann Corona in V-12. Lobate flow fronts associated with unit *fcI*, sourced from Ituana Corona (V-25), marks the northeast corner of the Llorona Planitia basin; one flow lobe of unit *fcI* embays unit *IL*.

Impact Craters

The Greenaway quadrangle (V-24) hosts 23 impact craters (table 1). Thirteen craters have diameters <20 km, eight range from 20 to 90 km diameter, and two show diameters >90 km. Only one crater (unnamed crater b, table 1) is tectonized; the rest of the craters do not appear deformed. Outflow material extending from Vigée-Lebrun crater flows around wrinkle ridges, clearly indicating that this crater postdates local wrinkle-ridge formation and regional contractional strain. Greenaway, Maria Celeste, and Vigée-Lebrun form multiring craters (Schaber and others, 1992); each contains segments of a discontinuous topographic ring composed of high-backscatter material located within the main crater basins. Other impact craters within the map area contain a central peak composed of high-radar-backscatter material. Fifteen craters have low-radar-backscatter interiors interpreted as interior fill (unit *cf*), five craters have high-radar-backscatter floors, and the backscatter within two craters is indeterminate.

Although all impact craters within the map area contain continuous ejecta blankets (unit *cu*), six craters also contain fluidized outflow material (unit *co*) (Asimow and Wood, 1992; Herrick and others, 1997). Outflow materials extending from craters Bourke-White, Maria Celeste, Vigée-Lebrun, and Wilder show low-radar backscatter and are segmented into complex channels approximately 1–2 km wide. Shield edifices and deposits associated with unit *st* locally cover outflow material associated with Wilder crater near lat 17° N., long 123° E. Outflow material extending from craters Ban Zhao and Himiko occurs as approximately 2–3 km wide, high-radar-backscatter lobate flows that extend as far as approximately 75 km from the respective ejecta blankets.

Extensive halos, including parabolas and splotches, are associated with some impact craters in the map area. Impact haloes are generally accepted as representing the distal, fine-grained component of impact ejecta, whereas parabolas represent material entrained by the prevailing easterly winds of the upper atmosphere (Campbell and others, 1992). Ban Zhao, Budveska, Himiko, and Olena craters are associated with well-developed, east-trending, low-radar-backscatter, parabolic halos. The Ban Zhao crater halo is superimposed on a second approximately 600 km diameter irregular halo that could be related to any of the five other impact craters located in the northeastern map area. In addition, Hwangcini and Phyllis craters show irregular, low-radar-backscatter halos. The one craterless splotch, located near lat 7° N., long 144° E., probably represents

a shock feature formed by the airburst of a meteor that failed to reach the surface (McKinnon and others, 1997). Although the paucity of impact craters on Venus inhibits dating of geologic units, the decay of crater halos may serve as an approximate index for the relative ages of individual craters (Izenberg and others, 1994; Basilevsky and Head, 2002). In addition, crater halos obscure local geologic relations in specific areas in the map area. For example, the Himiko crater halo hinders the identification of wrinkle ridges and possible flow material extending from Abundia and Nintu Coronae in the western map area.

Channels

Greenaway quadrangle (V-24) hosts both simple and complex channels (Baker and others, 1992). Simple channels, which consist of a long, single main channel, occur within units *st* and *fu*. Complex channels form anastomosing, braided, or distributary patterns and are associated with fluidized outflow (unit *co*) extending from some impact craters.

Simple Channels

Simple channels can be further subdivided into sinuous rilles and canali. Sinuous rilles are approximately 1–2 km wide, tens to hundreds of kilometers long, and extend from small (approximately kilometers in diameter) quasi-circular collapse regions (Baker and others, 1992). Sinuous rilles in the map area occur along a broad ridge associated with Rosmerta Corona and are discussed further in the Rosmerta Corona section. Canali, channels with consistent widths of 1–2 km for lengths as much as several hundred kilometers, occur across the lowland of V-24. The canali lack obvious sources, termini, and levee structures and appear to be negative topographic features. Ikhwezi Vallis, which extends into eastern Rusalka Planitia quadrangle (V-25), is a north-trending, segmented canale located in Llorona Planitia; segments are approximately 1 km wide and tens to hundreds of kilometers long. The segmented nature of Ikhwezi Vallis may be due to (1) covering by local volcanic flows, (2) subsurface fluid flow that eroded overlying surface materials (Lang and Hansen, 2006), or (3) partial roof collapse of a constructional lava tube (Gregg and Greeley, 1993). Kinsei Vallis, an approximately 50 km wide, east-west-trending canale, occurs in the vicinity of western Barbale Dorsa. Neither Ikhwezi nor Kinsei Valles are associated with definitive sources, termini, or any apparent flow material. Other unnamed canali in the map area are approximately hundreds of meters wide and as much as tens of kilometers long.

Complex Channels

Complex channels in the map area are associated with fluidized outflow material (unit *co*) extending from the impact craters Bourke-White, Maria Celeste, Vigée-Lebrun, and Wilder. Channels associated with these impact craters maintain relatively constant widths of 1–2 km and range in length from tens to hundreds of kilometers; each apparently facilitated transport of unit *co*. Low-radar-backscatter material marks the channel

floors, which are bounded by moderate-radar-backscatter walls or levees composed of unit *co*. These relations are consistent with at least a partial constructional origin for these complex channels.

Tectonic Features

Secondary structures including faults, fractures, ridges, and warps occur across the map area and display widely diverse scales, ranging from individual suites of linear to curvilinear features a few kilometers long to multiple suites of tectonic structures that define larger scale tectonic features such as coronae.

Wrinkle Ridges

Wrinkle ridges, low sinuous ridges 1–2 km wide and tens to hundreds of kilometers long that record a small degree of regional contractional strain occur on most terrestrial worlds, especially on large expanses of volcanic plains (Watters, 1988). At map scale, wrinkle ridges in the map area (V-24) describe a broad, east-northeast pattern across the north one-third of the map area, broadly paralleling Thetis Regio, and are interpreted as a response to loading of the lithosphere by Aphrodite Terra (Sandwell and others, 1997; Bilotti and Suppe, 1999). Wrinkle ridges within this northeastern trend typically contain wavelengths between approximately 25 and 50 km; however, shorter wavelengths of approximately 5 km are common within some coronae interiors. Based on mechanical considerations, shorter-wavelength suites likely reflect deformation of a thinner layer, and longer-wavelength suites likely reflect deformation of a thicker layer. Local variations from the east-northeastern trend exist at the ten- to hundred-kilometer scale. For example, at lat 18.5° N., long 131° E., wrinkle ridges define an arc around a quasi-circular topographic low northwest of Kubebe Corona.

In contrast to the rest of the map area, wrinkle ridges are rare in southeastern V-24. Only local east-west-trending, wrinkle-ridge suites occur over areas of approximately hundreds of kilometers. The relatively low strain preserved in southeastern V-24 may be attributed to strain partitioning or to burial by later-stage volcanic flows. Wrinkle ridges are also notably absent within exposures of unit *rtGH*, although wrinkle ridges extend to the boundary between the underlying ribbon-tessera terrain and the overlying shield terrain. These relations presumably indicate that unit *rtGH* is not rheologically amenable to wrinkle-ridge formation, whereas the thin layer of overlying shield terrain (unit *st*) can be readily deformed into wrinkle-ridge structures. Thus, the presence or absence of wrinkle ridges in the map area is likely related to rheological criteria rather than temporal considerations.

Linear Features

The Greenaway quadrangle (V-24) hosts numerous high-radar-backscatter, linear to curvilinear features. Although some of these features are too narrow to allow robust characterization, many contain parallel, low-radar-backscatter segments

indicating a trough-like character. We interpret most linear and curvilinear features as graben and fractures; where we cannot characterize the features as graben or fractures, we map the features as regional lineaments. Individual graben and fractures range in length from effective resolution (approximately 1–2 km) to hundreds of kilometers. Graben and fractures describe linear, radial, concentric, and anastomosing patterns. Radial and concentric fractures occur within coronae. Rosmerta and Blai Coronae, for example, display prominent suites of radial fractures and graben, whereas Abundia and Nintu Coronae host concentric fracture patterns. Coronae along the topographic arch are linked by a northerly trending, approximately 1,500 km long and approximately 500 km wide, anastomosing zone of fractures and graben.

Three other zones of linear features crop out in local topographic highs (approximately 100 m high) in the northwestern, central, and southeastern map area. The northwestern zone hosts northerly trending lineaments and fractures, approximately hundreds of kilometers long, immediately north of Abundia Corona. The central zone occurs in an approximately 200- by 250-km patch in the central map area along the east margin of the topographic arch. This zone consists of two suites of near orthogonal northwest- and northeast-trending fractures (wavelengths approximately 5–20 km). The southeastern zone is approximately 1,000 km wide and consists of northeast-trending lineaments, fractures, and graben, each having lengths of approximately tens to hundreds of kilometers, that cut the eastern extent of unit rtGH and extend from northeastern Thetis Regio quadrangle (V–36) to southwestern Rusalka Planitia quadrangle (V–25).

Coronae

Coronae are circular to quasi-circular features broadly defined by an annulus of fractures or ridges, an interior topographic depression or bulge, and possible radial fractures (Janes and others, 1992; Squyres and others, 1992; Stofan and others, 1992). “Corona” is a morphologic term stemming from the Latin word for crown (Stofan and others, 1997). However, the term “corona” has taken on a genetic connotation implying that any circular to elongate structure defined by an annulus of concentric fractures and (or) ridges is the result of the interaction of a diapir with the lithosphere (Squyres and others, 1992; Stofan and others, 1992; Koch and Manga, 1996; Smrekar and Stofan, 1997; Stofan and others, 1997; Chapman and Zimbelman, 1998; Chapman, 1999; DeLaughter and Jurdy, 1999; Hansen, 2003). Some studies, though, suggest that at least some coronae may result from other processes such as impact cratering (Schultz, 1992, 1993; Hamilton, 1993, 2005; Stewart and others, 1993; Vita-Finizi and others, 2005; McDaniel and Hansen, 2005). We do not endorse any particular model of corona formation. We qualitatively describe features in the map area that fit the morphologic description of a corona and visit the idea of various corona formation hypotheses in the Discussion section.

The Greenaway quadrangle (V–24) hosts seven coronae. Four coronae lie along the northeast-trending topographic arch and three coronae occur as isolated features in the west half of the map area. An eighth corona (Blai Corona) lies mostly within

the Thetis Regio quadrangle (V–36) to the south but extends into the southern map area. Rosmerta and Blai Coronae exhibit well-developed radial fractures, positive topography, and extensive radial flows. The other coronae are similar to old coronae of Chapman and Zimbelman (1998), consisting of low circular basins locally surrounded by raised rims and generally lacking obvious radial fractures or extensive volcanic flows. Each corona is discussed below.

Abundia Corona (lat 18° N., long 125° E.; approximately 300 km diameter) includes an approximately 75–100 km wide annulus of concentric fractures (fracture spacing approximately 1–2 km), locally covered by low-backscatter material. Along the north arc of the annulus, a suite of approximately 10–100 km long, north-trending lineaments and fractures (wavelength approximately 1–5 km) trend approximately perpendicular to the concentric fractures and are preserved in a broad topographic high. Relative timing between these two fracture suites is unconstrained, and it is unclear if the north-trending fractures and lineaments are associated with the formation of Abundia Corona. The annulus surrounds an approximately 150 km diameter circular basin. The basin contains shields and associated materials of unit st and a centrally located, approximately 100 km diameter dome. Wrinkle ridges that are approximately 50–100 km long and have wavelengths of approximately 10–15 km trend northeast through the basin, which is consistent with the regional trend, although wrinkle ridges within the basin exhibit shorter wavelengths. The large dome lacks wrinkle ridges. Two approximately 20 km diameter, steep-sided tholi, previously called “pancake domes” (McKenzie and others, 1992; Pavri and others, 1992), occur within the vicinity of Abundia Corona. One tholus lies superposed on the west edge of the annulus, whereas the second dome lies approximately 50 km east of the outer edge of the annulus.

Blai Corona (lat –0.4° N., long 134.5° E.) occurs predominantly within Thetis Regio quadrangle (V–36) south of the map area. Graben, >100 km long, radiate from the corona center and cut unit rtGH; the graben broadly parallel local ribbon-structure trends. Flow material sourced from Blai Corona (unit fbB) embays unit rtGH and floods local topographic lows, including ribbon structures, for as much as hundreds of kilometers.

Kamadhenu Corona (lat 20° N., long 136° E.; approximately 400 km diameter) includes a 30-km-wide, horseshoe-shaped ridge that has parallel fractures approximately 100 km long and approximately 1–5 km wide. The ridge is cut by an approximately 25 km diameter pit at lat 19.5° N., long 136.5° E. that is marked by an approximately 15 km wide annulus of concentric fractures. Local topographic highs as much as approximately 100 km² within the corona interior preserve two distinct lineament sets. One set consists of northeast-trending fractures approximately 1 km wide and 50–75 km long that have 10–15 km spacing. The second set consists of tightly spaced (<<1 km), northwest-trending lineaments similar to those within unit IL. Wrinkle ridges that are approximately 50–100 km long and have wavelengths of approximately 5–10 km trend northeast through the corona interior and parallel the regional wrinkle-ridge trend.

Kubebe Corona (lat 15° N., long 132° E.; approximately 150 km diameter) includes an approximately 50–75 km wide annulus of fractures that surround an approximately 75 km

diameter circular basin. Kubebe Corona corresponds with a northwest bend in the fracture zone along the topographic arch. Low-radar-backscatter material composed of shields and associated deposits of unit *st* mark the floor of the basin and locally cover north-trending fractures. High-radar-backscatter material, presumably volcanic flow material, extends from the east and west margins of the corona down the flanks of the topographic arch. Complete boundaries for the flow materials are obscured and difficult to trace in many locales, which makes identifying entire flow units difficult. As a result, we indicate flow boundaries and flow directions where possible. Adjacent to the northwest edge of Kubebe Corona is an approximately 25 km wide, quasi-circular ridge that surrounds an approximately 200 km wide circular basin that contains low-radar-backscatter material composed of shields and associated deposits. Approximately 100 km² patches of <1 km-spaced, north-trending lineaments crop out within the basin. The relation between Kubebe Corona and the adjacent corona-like feature is unclear. The adjacent feature may be genetically related to, or completely independent of, Kubebe Corona.

Nintu Corona (lat 19.5° N., long 123.5° E.; approximately 100 km diameter), located about 100 km west-northwest of Abundia Corona, consists of an approximately 30 km wide annulus of concentric fractures surrounding a 50-km-diameter, circular basin. The basin hosts an approximately 25 km diameter, low-backscatter, steep-sided, flat-topped dome resembling a tholus. A quasi-circular, approximately 15 km diameter dome crosscuts the annulus near lat 19° N., long 123° E.

Rosmerta Corona (lat 0.5° N., long 124° E.; approximately 300 km diameter) represents the best developed corona in the map area; Rosmerta Corona includes an approximately 25 km wide trough surrounding an approximately 125 km diameter, quasi-circular plateau covered with low- and moderate-backscatter material. A northerly trending fracture zone extends from Thetis Regio quadrangle (V–36) to the south and cuts through the trough, but it diverges around and surrounds the plateau and continues north, cutting unit *rtGH*. In western Rosmerta Corona, low- and moderate-radar-backscatter material fills the trough, locally covering parts of the fracture zone. A 50-km-wide, 200-km-long ridge occurs northwest of Rosmerta Corona. Three sinuous rilles occur on the northwest side of the ridge and are associated with minor amounts of flow material. Two of the rilles begin as a single conduit about 1 km wide and several kilometers long but branch into two <1-km-wide segments that are several kilometers long. A suite of northwest-trending fractures radiate from an area near lat 1.5° N., long 123° E. and extend about 400 km into unit *rtGH*.

Unnamed Corona a (lat 11.5° N., long 135.5° E.; approximately 150 km diameter) consists of a highly degraded, approximately 25 km wide, quasi-circular annulus that surrounds an interior topographic low. Moderate-radar-backscatter material extends radially for approximately 300 km from the annulus and embays a kipuka of unit *IL* near lat 11° N., long 138° E.

Unnamed corona b (lat 15° N., long 134.5° E.; approximately 100 km diameter) includes a 15-km-wide annulus of concentric fractures surrounding a 60-km-wide circular basin. Low-radar-backscatter material extends northeast from the topographic basin locally covering part of the annulus.

Dorsa

Dorsa define long-wavelength, linear topographic warps as much as thousands of kilometers long. The map area hosts three such features: Barbale Dorsa, Lumo Dorsa, and the northeast-trending topographic arch. Kipukas of unit *IL* decorate Barbale and Lumo Dorsa, whereas the northeast-trending topographic arch contains kipukas of unit *rtGH*, coronae fragments, and lineaments associated with unit *IL*.

Barbale Dorsa, northwest-trending dorsa in Llorona Planitia, exposes unit *IL* and is locally covered by unit *st*. Barbale Dorsa's low topographic expression, which extends to the resolution of the Magellan altimetry, makes accurately determining the margins and dimensions of Barbale Dorsa difficult.

Northwest-trending Lumo Dorsa occurs along the northeast slope of Llorona Planitia, where it extends into Vellamo Planitia quadrangle (V–12) and Rusalka Planitia quadrangle (V–25). Lumo Dorsa contains a core of unit *IL*. Northeast-trending wrinkle ridges that have wavelengths of 10–25 km cut Lumo Dorsa, whereas wrinkle ridges that have wavelengths of 5–10 km parallel the kipukas of unit *IL*. Unit *fcI*, sourced in adjacent V–25, embays Lumo Dorsa along its northeast edge. Young and Hansen (2003) suggested that the interaction of Lumo Dorsa with successive members of unit *fcI* records an extended progressive history of warp growth in the region.

The northeast-trending topographic arch has poorly defined margins but extends a total distance of approximately 2,500 km from about lat 9° N., long 133° E. in the map area to about lat 34° N., long 137° E. in V–12. The arch spans approximately 800 km and is covered by unit *st* and coronae-related flow material. As discussed above, fragments of four coronae connected by a northerly trending fracture zone occur along the arch. Kipukas of unit *rtGH* crop out as local topographic highs (approximately tens to hundreds of meters high) along the arch flanks and crest. Northwest-trending lineaments associated with unit *IL* also crop out along the arch.

Discussion

Geologic relations derived from mapping the Greenaway quadrangle (V–24) bear on some issues of global interest: ribbon-tessera terrain, coronae development, and the style and sources of volcanic resurfacing.

A major question in the map area is the genetic relation and spatial extent of ribbon-tessera terrain. Although ribbon-tessera terrain occurs as geographically isolated patches within the map area, the consistent structural trends among outcrops imply that all patches are remnants of the same unit, although we cannot robustly constrain its lateral extent. In addition, it is premature to state that ribbon-tessera terrain in the map area is part of a globally extensive unit as predicted by Basilevsky and Head (1998), Head and Basilevsky (1998), and Ivanov and Head (2001). Lineament trends within unit *IL* are broadly consistent across the map area with northwest structural trends within unit *rtGH*. The nature of this consistent trend is uncertain, but in some localities (near lat 22° N., long 123° E.), unit *IL* lineaments appear to grade into ribbon-tessera trends. In addition,

the area between lats 6°–11° N. and longs 136°–142° E. exhibits northwest-trending lineaments associated with unit IL (but outcrop within unit st) that parallel ribbon-tessera structure trends. Both cases reflect a possible genetic relation between ribbon-tessera terrain and unit IL, which suggests that unit IL represents either a structural facies within ribbon-tessera terrain or local reactivation of buried or veiled ribbon-tessera-related structures. These hypotheses may be tested by future mapping; it is possible that units rtGH and IL form a continuous unit across much of the map area, where they are obscured by a thin veil of shield terrain and other flow materials.

Coronae in the map area show variability in their morphology and range of associated structures, signifying that more than one mechanism might be responsible for the formation of coronae-like features. Structure patterns and topographic profiles of Rosmerta and Blai Coronae and the arch corona are consistent with current models that attribute coronae formation to Rayleigh-Taylor instabilities (Tackley and Stevenson, 1991) or mantle diapirs (Stofan and Head, 1990; Squyres and others, 1992; Stofan and others, 1992). Abundia and Nintu Coronae, however, are strikingly different from other coronae in the map area. Both coronae have amphitheater-like topographic profiles and lack obvious radial fractures, making them similar to circular lows (McDaniel and Hansen, 2005), although the possibility that the north-trending fractures located north of Abundia Corona may reflect locally preserved radial fractures cannot be excluded. The absence of obvious or at least extensive radial fractures may be attributed to burial by subsequently emplaced material and (or) the impairment of radial fracture formation due to a horizontal regional stress field (Withjack and Scheiner, 1982). However, if radial fractures formed during Abundia and (or) Nintu Coronae formation, the fractures would be expected to cut Gegute Tessera, yet no such structures are observed. Furthermore, if radial fracture formation is impaired due to an imposed stress field, the resulting structure should be elongate rather than circular (Withjack and Scheiner, 1982). Both Abundia and Nintu Coronae form almost perfectly circular structures. Therefore, we suggest that the formation of these two coronae is difficult to accommodate within the diapiric hypothesis. Instead, Abundia and Nintu Coronae may have formed from different processes, including caldera formation (Squyres and others, 1992; McDaniel and Hansen, 2005) or bolide impact (Schultz, 1992, 1993; Hamilton, 1993, 2005; Stewart and others, 1993; Vita-Finizi and others, 2005; McDaniel and Hansen, 2005), where the rheology of the target material has varied over time.

Shields and coronae are the two contributors to volcanic resurfacing in the map area. Shields associated with shield terrain (unit st) are the dominant volcanic source for resurfacing >70 percent of the map area. Coronae-sourced materials resurface only about 5 percent of the map area. Shield-sourced resurfacing is distinct from resurfacing styles in the adjacent quadrangles (V–25, Young and Hansen, 2003; V–35, Bleamaster and Hansen, 2005; V–37, Hansen and DeShon, 2002), where volcanic activity is associated with coronae and chasmata evolution. Stofan and others (2005) recognized shields as a major contributor to volcanic resurfacing in other lowland regions of Venus, which, when combined with Hansen (2005) and this study, suggests that shield-sourced volcanism may

play a significantly larger role in Venus resurfacing than previously recognized. Further, volcanic resurfacing in the map area appears to be inconsistent with the proposed catastrophic resurfacing event of Strom and others (1994; see Hansen, 2005, and Hansen and Young, 2006, for a more complete discussion). According to the catastrophic resurfacing hypothesis, Venus' lowlands, including the map area, were resurfaced with flood-type lava flows approximately 750 Ma. The basis for this proposal is the paucity of impact craters on Venus' surface (Strom and others, 1994). Specifically, in order to erase or bury pre-existing impact craters, volcanic material (Banerdt and others, 1997) approximately 1–3 km thick must have been emplaced in Venus' lowlands at a geologically rapid (10–100 m.y.) rate (Ivanov and Head, 1996; Basilevsky and others, 1997; Head and Coffin, 1997; Head and Basilevsky, 1998). If 1- to 3-km-thick lavas were emplaced, then map relations should show abrupt, steep contacts between resurfacing material and pre-existing topography; the flood lavas also should reside unconformably on basement materials (units rtGH, IL). Although volcanic flow materials in the map area do appear to reside unconformably on basement materials (units rtGH, IL), they appear to be relatively thin layers (as much as hundreds of meters?) that maintain extremely shallow contacts with the basement materials. The thin nature of the volcanic materials in the map area, therefore, suggests that they could not have erased pre-existing impact craters, which makes it seem unlikely that catastrophic resurfacing occurred within the map area. However, the observation that the majority of impact craters in the map area occur on units located within the lowlands and not on the higher-standing unit rtGH suggests that resurfacing may have been relatively rapid, although it would not have been specifically voluminous. If pre-existing impact craters have been erased in the map area, it may have been through processes other than burial (Hansen, 2006).

Geologic History

Geologic unit correlation is the process of interpreting mutual time relations of local stratigraphic sections, and it attempts to synthesize local stratigraphic sections into a composite time scheme applicable to a wider region (Dunbar and Rogers, 1957). The surest means to correlate units involves one or more criteria: fossil content, isotopic data, stratigraphic position in relation to a widespread geologically instantaneous marker bed (Compton, 1985; Prothero, 1990), and significant and robust impact crater statistics (Hauck and others, 1998; Campbell, 1999). The inability to robustly ascertain any of these criteria on Venus makes geologic unit correlation highly suspect. Therefore, we developed a Sequence of Map Units (SOMU) for the Greenaway quadrangle (V–24), using embayment and crosscutting relations to constrain relative timing and allow an interpretation of a geologic history. Because of the widespread occurrence of many units in the map area (notably the terrains), we do not divide the SOMU into geographic regions.

The geologic history of the map area supports the interpretation that, as is the case on most of Venus, volcanism and

tectonism are the two dominant processes that have shaped the map area, although determining the timing of specific events in the map area is nontrivial. Based on embayment and crosscutting relations, ribbon-tessera terrain (unit rtGH) and lineated terrain (unit IL) appear to be two of the oldest recorded units in the Greenaway quadrangle (V–24), where the emplacement history and timing of deformation of these two units is unconstrained. The temporal relation between the two units is also unconstrained, but, as discussed earlier, it is possible that units rtGH and IL are genetically related, which would infer that these two units are closely related in time. The occurrence of unit ibGH in intratessera basins implies that unit ibGH cannot be older than ribbon-tessera terrain formation. In turn, the absence of tessera-related structures that cut unit ibGH suggests that the emplacement of unit rtGH material continued after the formation of unit ibGH. Because unit ibGH is only in contact with unit rtGH, the temporal relation of unit ibGH to other map units is unconstrained. Where units st and fu are in contact with ribbon-tessera terrain and lineated terrain, they are stratigraphically younger than units rtGH and IL. Thus, units st and fu at any one location postdate the formation of units rtGH and (or) IL at that same location. However, given the uncertainty of the extent of units rtGH and IL in the subsurface across the map area, we cannot robustly state (or deny) that all of units st and fu postdate the formation of all of units rtGH and IL. In addition, units st and fu appear to have time-transgressive relations with the other map units. Warping of the Gegute Tessera inlier postdated unit rtGH and unit IL formation, but timing cannot be further constrained because there is no evidence that any other map units were concurrently warped. Scattered outcrops of units rtGH and IL along the topographic arch indicate that they predate arch formation, suggesting that the uplift of the arch is responsible for local preservation of the two terrain units. The topographic arch and the arch-related coronae (including the anastomosing fracture zone linking the coronae) probably formed synchronously. To suggest differently would require an explanation for the parallelism of the arch and coronae along the arch crest. Initiation of arch coronae volcanism is unconstrained, however. Some coronae flow material extends down the arch flanks, indicating that coronae-related volcanism occurred, at least locally, after arch formation.

Because material flow units are not in contact with each other, their temporal relations cannot be constrained. However, their interactions with units rtGH and IL and (or) topography do provide some time constraints. The parallelism of units fcA, fcR, and fcS with the trend of the western basin implies that these three flow units postdate formation of the topographic arch and, therefore, units rtGH and IL, which is an interpretation that is consistent with unit fcS embayment of units rtGH and IL and unit fcR embayment of unit rtGH. Because unit rtGH is similarly embayed by unit fcB, Blai Corona flow material is likely younger than ribbon-tessera terrain, although the possibility that Rosmerta and Blai Coronae occurred (and initially emplaced flow material) synchronously with ribbon-tessera terrain formation cannot be excluded. Embayment relations also indicate that unit fcI is younger than unit IL. The timing of unit fc cannot be robustly constrained based on direct observations of the surface geology but, instead, requires inferences regard-

ing the subsurface geology. For example, if unit rtGH and (or) unit IL extend in the subsurface to the southeast corner of the map area, then unit fc must be younger than one or both of these terrain units. However, if neither terrain unit exists in the subsurface in the southeast corner, then the timing of unit fc is unconstrained and it may be younger than, concurrent with, or older than units rtGH and (or) IL.

Formation of the fracture zone in the southeastern map area appears to have occurred time transgressively with unit st. However, because the fracture zone cuts unit rtGH near lat 1° N., long 139° E., it must locally postdate unit rtGH.

Wrinkle ridges and impact craters are some of the youngest features within the map area. This interpretation is based on the observations that wrinkle ridges deform, and most impact craters occur on, units in the lowlands; the impact crater Wilder is embayed by shield-related deposits, suggesting that Wilder is locally younger than unit st. However, initiation of wrinkle-ridge formation is difficult to constrain. The initial age of imposition of a wrinkle-ridge fabric may predate its current geomorphic expression, implying that there is ideally no stratigraphic constraint on wrinkle-ridge timing; material units can only be said to predate the very last phase of wrinkle-ridge formation. Further, the observation that, with the exception of unnamed crater b, impact craters are not deformed suggests that impact craters in this map area are younger than wrinkle ridges. This observation also suggests that relatively little tectonism has occurred in the map area since impact-crater formation.

The Greenaway quadrangle (V–24) records a rich geologic history for parts of Venus' lowland and highland regions. The geologic history is constrained by observed contact and structural interactions, which resulted in the construction of a Sequence of Map Units consistent with the 1:5,000,000 scale of mapping. Mapping at a larger scale that shows a higher degree of detail may lead to the discovery of new relations inconsistent with our mapping. Map users are encouraged to analyze regions of interest with specific questions in mind.

References Cited

- Arvidson, R.E., Greeley, R., Malin, M.C., and 5 others, 1992, Surface modification of Venus as inferred from Magellan observations of plains: *Journal of Geophysical Research*, v. 97, p. 13,303–13,317.
- Asimow, P.D., and Wood, J.A., 1992, Fluid outflows from Venus impact craters—Analysis from Magellan data: *Journal of Geophysical Research*, v. 97, p. 13,643–13,665.
- Aubele, J.C., 1996, Akkriva small shield plains—Definition of a significant regional plains unit on Venus [abs.], *in* Lunar and Planetary Science Conference XXVII: Houston, Tex., Lunar and Planetary Institute, p. 49.
- Baker, V.R., Komatsu, G., Parker, T.J., and 3 others, 1992, Channels and valleys on Venus—Preliminary analysis of Magellan data: *Journal of Geophysical Research*, v. 97, p. 13,421–13,444.
- Banerdt, W.B., McGill, G.E., and Zuber, M.T., 1997, Plains tectonics on Venus, *in* Bougher, S.W., Hunten, D.M., and

- Phillips, R.J., eds., *Venus II*: Tucson, University of Arizona Press, p. 901–930.
- Banks, B.K., and Hansen, V.L., 2000, Relative timing of crustal plateau magmatism and tectonism at Tellus Regio, Venus: *Journal of Geophysical Research*, v. 105, p. 17,655–17,667.
- Basilevsky, A.T., and Head, J.W., 1998, The geologic history of Venus—A stratigraphic view: *Journal of Geophysical Research*, v. 103, p. 531–8544.
- Basilevsky, A.T., and Head, J.W., 2002, Venus—Timing and rates of geologic activity: *Geology*, v. 30, p. 1015–1018.
- Basilevsky, A.T., Head, J.W., Schaber, G.G., and Strom, R.G., 1997, The resurfacing history of Venus, *in* Bougher, S.W., Hunten, D.M., and Phillips, R.J., eds., *Venus II*: Tucson, University of Arizona Press, p. 1047–1084.
- Bilotti, F., and Suppe, J., 1999, The global distribution of wrinkle ridges on Venus: *Icarus*, v. 139, p. 137–157.
- Bindschadler, D.L., and Head, J.W., 1991, Tessera terrain, Venus—Characterization and models for origin and evolution: *Journal of Geophysical Research*, v. 96, p. 5889–5907.
- Bindschadler, D.L., Schubert, G., and Kaula, W.M., 1992, Cold-spots and hotspots—Global tectonics and mantle dynamics on Venus: *Journal of Geophysical Research*, v. 97, p. 13,495–13,532.
- Bleamaster, L.F., and Hansen, V.L., 2005, Geologic map of the Ovda Regio quadrangle (V–35), Venus: U.S. Geological Survey Geologic Investigations Series I–2808, scale 1:5,000,000.
- Brown, C.D., and Grimm, R.E., 1997, Tessera deformation and the contemporaneous thermal state of the plateau highlands, Venus: *Earth and Planetary Science Letters*, v. 147, p. 1–10.
- Bullock, M.A., and Grinspoon, D.H., 1996, The stability of climate on Venus: *Journal of Geophysical Research*, v. 101, p. 7521–7530.
- Campbell, B.A., 1999, Surface formation rates and impact crater densities on Venus: *Journal of Geophysical Research*, v. 104, p. 1897–1916.
- Campbell, D.B., Stacy, N.J.S., Newman, W.I., and 5 others, 1992, Magellan observations of extended impact crater related features on the surface of Venus: *Journal of Geophysical Research*, v. 97, p. 16,249–16,277.
- Chapman, M.G., 1999, Geologic/geomorphic map of the Galindo quadrangle (V–40), Venus: U.S. Geological Survey Geologic Investigation Series I–2613, scale 1:5,000,000.
- Chapman, M.G., and Zimbelman, J.R., 1998, Corona associations and their implications for Venus: *Icarus*, v. 132, p. 344–361.
- Compton, R.R., 1985, *Geology in the field*: New York, Wiley and Sons, 398 p.
- Crisp, D., and Titov, D., 1997, The thermal balance of the Venus atmosphere, *in* Bougher, S.W., Hunten, D.M., and Phillips, R.J., eds., *Venus II*: Tucson, University of Arizona Press, p. 353–384.
- Crumpler, L.S., Aubele, J.C., Senske, D.A., and 3 others, 1997, Volcanoes and centers of volcanism on Venus, *in* Bougher, S.W., Hunten, D.M., and Phillips, R.J., eds., *Venus II*: Tucson, University of Arizona Press, p. 697–756.
- DeLaughter, J.E., and Jurdy, D.M., 1999, Corona classification by evolutionary stage: *Icarus*, v. 139, p. 81–92.
- Donahue, T.M., 1999, New analysis of hydrogen and deuterium escape from Venus: *Icarus*, v. 141, p. 226–245 (doi: 10.1006/icar.1999.6186).
- Donahue, T.M., Grinspoon, D.H., Heartle, R.E., and Hodges, R.R., Jr., 1997, Ion/neutral escape of hydrogen and deuterium—Evolution of water, *in* Bougher, S.W., Hunten, D.M., and Phillips, R.J., eds., *Venus II*: Tucson, University of Arizona Press, p. 385–414.
- Donahue, T.M., Hoffman, J.H., Hodges, R.R., and Watson, A.J., 1982, Venus was wet—A measurement of the ratio of deuterium to hydrogen: *Science*, v. 216, p. 630–633.
- Donahue, T.M., and Russell, C.T., 1997, The Venus atmosphere and ionosphere and their interaction with the solar wind—An overview, *in* Bougher, S.W., Hunten, D.M., and Phillips, R.J., eds., *Venus II*: Tucson, University of Arizona Press, p. 3–31.
- Dunbar, C.O., and Rogers, J., 1957, *Principles of stratigraphy*: New York, Wiley and Sons, 356 p.
- Fegley, B., Jr., Klingelhofer, G., Lodders, K., Widemann, T., 1997, Geochemistry of surface-atmosphere interactions on Venus, *in* Bougher, S.W., Hunten, D.M., and Phillips, R.J., eds., *Venus II*: Tucson, University of Arizona Press, p. 591–636.
- Ford, J.P., Plaut, J.J., Weitz, C.M., and 5 others, 1993, *Guide to Magellan image interpretation*: National Aeronautics and Space Administration Jet Propulsion Laboratory Publication, 287 p.
- Ghent, R.R., and Hansen, V.L., 1999, Structural and kinematic analysis of eastern Ovda Regio, Venus—Implications for crustal plateau formation: *Icarus*, v. 139, p. 116–136.
- Ghent, R.R., and Tibuleac, I.M., 2002, Ribbon spacing in Venusian tessera—Implications for layer thickness and thermal state: *Geophysical Research Letters*, v. 29.
- Gilmore, M.S., Collins, G.S., Ivanov, M.A., Marinangeli, L., and Head, J.W., 1998, Style and sequence of extensional structures in tessera terrain, Venus: *Journal of Geophysical Research*, v. 103, p. 16,813–16,840.
- Gilmore, M.S., and Head, J.W., 1994, Intratessera volcanism of Alpha and Tellus Tesserae on Venus [abs.], *in* Lunar and Planetary Science Conference XXVII: Houston, Tex., Lunar and Planetary Institute, p. 425–426.
- Greeley, R., Arvidson, R., Elachi, C., and 8 others, 1992, Aeolian features on Venus—Preliminary Magellan results: *Journal of Geophysical Research*, v. 97, p. 13,319–13,345.
- Gregg, T.K.P., and Greeley, R., 1993, Formation of Venusian canals—Consideration of lava types and their thermal behaviors: *Journal of Geophysical Research*, v. 98, E6, p. 10,873–10,882.
- Grimm, R.E., and Hess, P.C., 1997, The crust of Venus, *in* Bougher, S.W., Hunten, D.M., and Phillips, R.J., eds., *Venus II*: Tucson, University of Arizona Press, p. 1205–1244.
- Guest, J.E., Bulmer, M.H., Aubele, J., and 6 others, 1992, Small volcanic edifices and volcanism in the plains of Venus:

- Journal of Geophysical Research, v. 97, p. 15,949–15,966.
- Hamilton, W.B., 1993, Evolution of Archean mantle and crust, *in* Reed, J.C., Jr, Ball, T.T., Farmer, G.L., and Hamilton, W.B. eds., Precambrian-conterminous United States: Geological Society of America, Geology of North America, C-2, p. 597–614.
- Hamilton, W.B., 2005, Plumeless Venus has ancient impact-accretionary surface, *in* Foulger, G.R., Natland, J.H., Presnall, D.C., and Anderson, D.L., eds., Plates, Jumes and paradigms: Geological Society of America, Special Paper 388, p. 781–814.
- Hansen, V.L., 2000, Geologic mapping of tectonic planets: Earth and Planetary Science Letters, v. 176, p. 527–542.
- Hansen, V.L., 2003, Venus diapirs—Thermal or compositional?: Geological Society of America Bulletin, v. 115, p. 1040–1052.
- Hansen, V.L., 2005, Venus's shield terrain: Geological Society of America Bulletin, v. 117, p. 808–812.
- Hansen, V.L., 2006, Geologic constraints on crustal plateau surface histories, Venus—The lava pond and bolide impact hypotheses: Journal of Geophysical Research, v. 111, no. E11010 (doi:10.1029/2006JE002714).
- Hansen, V.L., 2009, Geologic Map of Niobe Planitia quadrangle (V–23), Venus: U.S. Geological Survey Scientific Investigations Map 3025, scale 1:5,000,000.
- Hansen, V.L., and DeShon, H.R., 2002, Geologic map of the Diana Chasma quadrangle (V–37), Venus: U.S. Geological Survey Geologic Investigations Series Map I–2752, scale 1:5,000,000.
- Hansen, V.L., and Willis, J.J., 1996, Structural analysis of a sampling of tesserae—Implications of Venus geodynamics: Icarus, v. 123, p. 296–312.
- Hansen, V.L., and Willis, J.J., 1998, Ribbon terrain formation, southwestern Fortuna Tessera, Venus—Implications for lithosphere evolution: Icarus, v. 132, p. 332–343.
- Hansen, V.L., Willis, J.J., and Banerdt, W.B., 1997, Tectonic overview and synthesis, *in* Bougher, S.W., Hunten, D.M., and Phillips, R.J., eds., Venus II: Tucson, University of Arizona Press, p. 794–844.
- Hauck, S.A., Phillips, R.J., and Price, M.H., 1998, Venus-crater distribution and plains resurfacing models: Journal of Geophysical Research, v. 103, p. 13,635–13,642.
- Head, J.W., and Basilevsky, A.T., 1998, Sequence of tectonic deformation in the history of Venus—Evidence from global stratigraphic relationships: Geology, v. 26, p. 35–38.
- Head, J.W., and Coffin, M.F., 1997, Large igneous provinces—A planetary perspective, *in* Mahoney, J.J., and Coffin, M.F., eds., Large Igneous Provinces—Continental, oceanic, and planetary flood volcanism: Washington, D.C., American Geophysical Union Geophysical Monograph Series, p. 411–438.
- Head, J.W., Crumpler, L.S., Aubele, J.C., Guest, J.E., and Saunders, R.S., 1992, Venus volcanism—Classification of volcanic features and structures, associations, and global distribution from Magellan data: Journal of Geophysical Research, v. 97, p. 13,153–13,197.
- Herrick, R.R., Sharpton, V.L., Malin, M.C., Lyons, S.N., Feely, K., 1997, Morphology and morphometry of impact craters, *in* Bougher, S.W., Hunten, D.M., and Phillips, R.J., eds., Venus II: Tucson, University of Arizona Press, p. 1,015–1,046.
- Hunten, D.M., 2002, Exospheres and planetary escape, *in* Mendillo, M., Nagy, A., and Waite, J.H., Atmospheres in the solar system—Comparative aeronomy: American Geophysical Union, Geophysical Monograph 130, p. 191–202.
- Ivanov, M.A., and Head, J.W., 1996, Tessera terrain on Venus—A summary of the global distribution, characteristics, and relation to surrounding units from Magellan data: Journal of Geophysical Research, v. 101, p. 14,861–14,908.
- Ivanov, M.A., and Head, J.W., 2001, Geology of Venus—Mapping of a geotraverse at 30° N. latitude: Journal of Geophysical Research, v. 106, p. 17,515–17,566.
- Izenberg, N.R., Arvidson, R.E., and Phillips, R.J., 1994, Impact degradation on Venusian plains: Geophysical Research Letters, v. 21, p. 289–292.
- Janes, D.M., Squyres, S.W., Bindschadler, D.L., and 4 others, 1992, Geophysical models for the formation and evolution of coronae on Venus: Journal of Geophysical Research, v. 97, E8, p. 16,055–16,067.
- Jones, A.P., and Pickering, K.T., 2003, Evidence for aqueous fluid-sediment transport and erosional processes on Venus: Journal Geological Society of London, v. 160, p. 319–327.
- Kirk, R.L., Soderblom, L.A., and Lee, E.M., 1992, Enhanced visualization for interpretation of Magellan radar data—Supplement to the Magellan special issue: Journal of Geophysical Research, v. 97, p. 16,371–16,380.
- Lang N. P. and Hansen, V.L., 2006, Venusian channel formation as a subsurface process: Journal of Geophysical Research, v. 111 (doi:10.1029/2005JE002629).
- Koch, D.M. and Manga, M., 1996, Neutrally buoyant diapirs—A model for Venus coronae: Geophysics Research Letters, v. 23, p. 225–228.
- Kumar, P.S., 2005, An alternative kinematic interpretation of Thetis Boundary Shear Zone, Venus—Evidence for strike-slip ductile duplexes: Journal of Geophysical Research, v. 110, no. E07001 (doi:10.1029/2004JE002387).
- Mackwell, S.J., Zimmerman, M.E., and Koldstedt, D.L., 1998, High-temperature deformation of dry diabase with applications to tectonics on Venus: Journal of Geophysical Research, v. 102, p. 975–984.
- Masursky, H., Elias, E., Ford, P.G., and 4 others, 1980, Pioneer Venus radar results—Geology from images and altimetry: Journal of Geophysical Research, v. 85, p. 8232–8260.
- McDaniel, K., and Hansen, V.L., 2005, Circular lows—A genetically distinct subset of coronae [abs.], *in* Lunar and Planetary Science Conference XXXVI: Houston, Tex., Lunar and Planetary Institute [CD-ROM].
- McKenzie, D., Ford, P.G., Liu, F., and Pettengill, G.H., 1992, Pancake-like domes on Venus: Journal of Geophysical Research, v. 97, p. 15,967–15,976.
- McKinnon, W.B., Zahnle, K.J., Ivanov, B.A., and Melosh, H.J., 1997, Cratering on Venus—Models and observations, *in* Bougher, S.W., Hunten, D.M., and Phillips, R.J., eds., Venus II: Tucson, University of Arizona Press, p. 969–1,014.
- Nordberg, T.L., Brewer, A., and Hansen, V.L., 2005, Detailed

- geologic mapping of Venus' crustal plateaus and implications for plateau formation: Geological Society of America Abstracts with Programs, v. 37, no. 7, p. 90.
- Pavri, B., Head, J.W., Kloze, K.B., and Wilson, L., 1992, Steep-sided domes on Venus—Characteristics, geologic setting, and eruption conditions from Magellan data: *Journal of Geophysical Research*, v. 97, p. 13,445–13,478.
- Phillips, R.J., Bullock, M.A., and Hauck, S.A., II, 2001, Climate and interior coupled evolution on Venus: *Geophysical Research Letters*, v. 28, p. 1779–1782.
- Phillips, R.J., and Hansen, V.L., 1994, Tectonic and magmatic evolution of Venus: *Annual Reviews of Earth and Planetary Science*, v. 22, p. 597–654.
- Prothero, D.R., 1990, *Interpreting the stratigraphic record*: New York, W.H. Freeman and Company, 410 p.
- Sandwell, D.T., Johnson, C.L., and Suppe, J., 1997, Driving forces for limited tectonics on Venus: *Icarus*, v. 129, p. 232–244.
- Schaber, G.G., Strom, R.G., Moore, H.J., and 7 others, 1992, Geology and distribution of impact craters on Venus—What are they telling us?: *Journal of Geophysical Research*, v. 97, p. 13,257–13,301.
- Schultz, P.H., 1992, Atmospheric effects on ejecta emplacement and crater formation on Venus from Magellan: *Journal of Geophysical Research*, v. 97, p. 16,183–16,248.
- Schultz, P.H., 1993, Searching for ancient Venus [abs.] in *Lunar and Planetary Science Conference XXIV*: Houston, Tex., Lunar and Planetary Institute.
- Skinner, J.A., and Tanaka, K.L., 2003, How should planetary map units be defined? [abs.], in *Lunar and Planetary Science Conference XXXIV*: Houston, Tex., Lunar and Planetary Institute [CD-ROM].
- Smrekar, S.E., and Stofan, E.R., 1997, Corona formation and heat loss on Venus by coupled upwelling and delamination: *Science*, v. 277, p. 1289–1294.
- Squyres, S.W., Janes, D.M., Baer, G., and 4 others, 1992, The morphology and evolution of coronae on Venus: *Journal of Geophysical Research*, v. 97, p. 13,3611–13,364.
- Stewart, C.A., Rampino, M.R., and Robinson, C.A., 1993, Impact shocks in the transition zone—Enough energy to trigger a plume? Venus coronae linked to missing population of large Venus impact craters?: *Eos, Transactions of the American Geophysical Union*, Supplement, Oct. 26, p. 80.
- Stofan, E.R., Brian, A.W., and Guest, J.E., 2005, Resurfacing styles and rates on Venus—Assessment of 18 Venusian quadrangles: *Icarus*, v. 173, p. 312–321.
- Stofan, E.R., Hamilton, V.E., Janes, D.M., and Smrekar, S.E., 1997, Coronae on Venus—Morphology and origin, in Bougher, S.W., Hunten, D.M., and Phillips, R.J., eds., *Venus II: Tucson*, University of Arizona Press, p. 931–965.
- Stofan, E.R., and Head, J.W., 1990, Coronae of Mnemosyne Regio, Venus—Morphology and origin: *Icarus*, v. 83, p. 216–243.
- Stofan, E.R., Sharpton, V.L., Schubert, G., and 4 others, 1992, Global distribution and characteristics of coronae and related features on Venus—Implications for origin and relation to mantle processes: *Journal of Geophysical Research*, v. 97, p. 13,347–13,378.
- Strom, R.G., Schaber, G.G., and Dawson, D.D., 1994, The global resurfacing of Venus: *Journal of Geophysical Research*, v. 99, p. 10,899–10,926.
- Tackley, P.J., and Stevenson, D.J., 1991, The production of small Venusian coronae by Rayleigh-Taylor instabilities in the uppermost mantle: *Eos, Transactions of the American Geophysical Union*, v. 72, p. 287.
- Tanaka, K.L., Moore, H.J., Schaber, G.G., and 9 others, 1994, *The Venus geologic mappers' handbook*: U.S. Geological Survey Open-File Report 94-438, 68 p.
- Tuckwell, G.W., and Ghail, R.C., 2003, A 400-km-scale strike-slip zone near the boundary of Thetis Regio, Venus: *Earth and Planetary Science Letters*, v. 211, p. 45–55.
- Vita-Finizi, C., Howarth, R.J., Tapper, S., and Robinson, C., 2005, Venusian craters, size distribution, and the origin of coronae, in Foulger, G.R., Natland, J.H., Presnall, D.C., Anderson, D.L., eds., *Plates, plumes and paradigms*: Geological Society of America, Special Paper 388, p. 815–824.
- Watters, T.R., 1988, Wrinkle ridge assemblages on the terrestrial planets: *Journal of Geophysical Research*, v. 93, p. 10,236–10,254.
- Wilhelms, D.E., 1990, Geologic mapping, in Greeley, R., and Batson, R.M., eds., *Planetary mapping*: New York, Cambridge University Press, p. 208–260.
- Withjack, M.O., and Scheiner, C., 1982, Fault patterns associated with domes—An experimental and analytical study: *American Association of Petroleum Geologists Bulletin*, v. 66, p. 302–316.
- Young, D.A., and Hansen V.L., 2003, Geologic map of the Rusalka Planitia quadrangle (V-25), Venus: U.S. Geological Survey Geologic Investigations Series I-2783, scale 1:5,000,000.
- Zimbelman, J.R., 2001, Image resolution and evaluation of genetic hypotheses for planetary landscapes: *Geomorphology*, v. 37, p. 179–199.

Table 1. Crater data for the Greenaway quadrangle (V-24), Venus.

Crater name	Unit label	Center latitude (deg N.)	Center longitude (deg E.)	Diameter (km)	Floor ¹	Halo ²	Deformation ³
Afua	st, ltL	15.5	124	0.011	LBS	N	N
Aimee	fcA	16.1	127.2	16.8	LBS	N	N
Ban Zhao	fu, rtGH, ltL	17.2	146.9	38.3	HBS	Y	N
Bourke-White	fu	21.1	147.9	34.4	LBS	N	N
Budevaska	st	0.5	143.2	18.7	HBS	Y	N
Callirhoe	st	21.2	140.7	32.9	LBS	IND	N
Escoda	fu, fcl	18.2	149.5	19.5	HBS	IND	N
Greenaway	fu	22.9	145.1	92.3	HBS	IND	N
Himiko	fu	19	124.3	36.7	HBS	Y	N
Hwangcini	st	6.3	141.7	30.8	LBS	Y	N
Jutta	st	0.0	142.6	7.0	LBS	N	N
Maria Celeste	st	23.4	140.4	96.6	LBS	IND	N
Neeltje	st	12.4	124.5	10.3	IND	N	N
Němcová	fcR	5.9	125.1	21.4	LBS	N	N
Ogulbek	st	2.4	145.1	6.6	LBS	N	N
Olena	fu	10.9	149	0.007	LBS	Y	N
Phyllis	st	12.2	132.4	10.6	LBS	Y	N
Tinyl	st	9.7	132.1	11.7	LBS	N	N
Vigée-Lebrun	st, ltL	17.3	141.4	57.6	LBS	IND	N
Wilder	rtGH, st	17.4	122.6	35.3	LBS	N	N
Unnamed crater a	st	8.0	148	<1	IND	N	N
Unnamed crater b	st	2.1	148.1	<1	LBS	N	Y
Unnamed crater c	st	11.9	132.4	<1	IND	N	N

¹Indicates the radar characteristic of the floor: HBS, high backscatter²Indicates whether halo is evident: N, no; Y, yes; IND, indeterminate³Indicates whether ejecta, rim, or outflow are cut by later tectonic structures: N, no; Y, yes